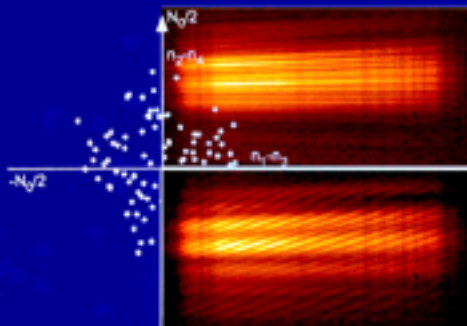


An Introduction to **Optical Stellar Interferometry**



**A. Labeyrie, S. G. Lipson,
and P. Nisenson**

CAMBRIDGE

CAMBRIDGE

www.cambridge.org/9780521828727

This page intentionally left blank

AN INTRODUCTION TO OPTICAL STELLAR INTERFEROMETRY

During the last two decades, optical stellar interferometry has become an important tool in astronomical investigations requiring spatial resolution well beyond that of traditional telescopes. This is the first book to be written on the subject. The authors provide an extended introduction discussing basic physical and atmospheric optics, which establishes the framework necessary to present the ideas and practice of interferometry as applied to the astronomical scene. They follow with an overview of historical, operational and planned interferometric observatories, and a selection of important astrophysical discoveries made with them. Finally, they present some as-yet untested ideas for instruments both on the ground and in space which may allow us to image details of planetary systems beyond our own.

This book will be used by advanced students in physics, optics, and astronomy who are interested in the ideas and implementations of astronomical interferometry.

ANTOINE LABEYRIE is Professor at the Collège de France. During his distinguished career he has made many fundamental contributions to high-resolution optical astronomy.

STEPHEN G. LIPSON is Chair of Electro-Optics and Professor of Physics at Technion–Israel Institute of Technology, Haifa. He is co-author of *Optical Physics, 3rd Edition* (Cambridge University Press, 1995).

PETER NISENSEN (1941–2004) studied physics and optics before becoming a professional astronomer at the Harvard Smithsonian Center for Astrophysics. His achievements include developing image detectors that can measure individual photon events.

AN INTRODUCTION TO OPTICAL STELLAR INTERFEROMETRY

A. LABEYRIE, S. G. LIPSON, AND P. NISENSEN



CAMBRIDGE
UNIVERSITY PRESS

CAMBRIDGE UNIVERSITY PRESS

Cambridge, New York, Melbourne, Madrid, Cape Town, Singapore, São Paulo

Cambridge University Press

The Edinburgh Building, Cambridge CB2 2RU, UK

Published in the United States of America by Cambridge University Press, New York

www.cambridge.org

Information on this title: www.cambridge.org/9780521828727

© A. Labeyrie, S. G. Lipson, and P. Nisenson 2006

This publication is in copyright. Subject to statutory exception and to the provision of relevant collective licensing agreements, no reproduction of any part may take place without the written permission of Cambridge University Press.

First published in print format 2006

ISBN-13 978-0-511-22286-3 eBook (Adobe Reader)

ISBN-10 0-511-22286-6 eBook (Adobe Reader)

ISBN-13 978-0-521-82872-7 hardback

ISBN-10 0-521-82872-4 hardback

ISBN-10 0-521-53565-4

Cambridge University Press has no responsibility for the persistence or accuracy of URLs for external or third-party internet websites referred to in this publication, and does not guarantee that any content on such websites is, or will remain, accurate or appropriate.

Contents

<i>List of Illustrations</i>	page xii
<i>Preface</i>	xxviii
1 Introduction	1
1.1 Historical introduction	1
1.2 About this book	7
<i>References</i>	7
2 Basic concepts: a qualitative introduction	9
2.1 A qualitative introduction to the basic concepts and ideas	9
2.1.1 Young's experiment (1801–3)	9
2.1.2 Using Young's slits to measure the size of a light source	11
2.2 Some basic wave concepts	13
2.2.1 Plane waves	15
2.2.2 Huygens' principle	15
2.2.3 Superposition	17
2.3 Electromagnetic waves and photons	19
<i>References</i>	22
3 Interference, diffraction and coherence	23
3.1 Interference and diffraction	23
3.1.1 Interference and interferometers	24
3.1.2 Diffraction using the scalar wave approximation	28
3.1.3 Fraunhofer diffraction patterns of some simple apertures	31
3.1.4 The point spread function	37
3.1.5 The optical transfer function	39
3.2 Coherent light	40
3.2.1 The effect of uncertainties in the frequency and wave vector	40
3.2.2 Coherent light and its importance to interferometry	41
3.2.3 Partial coherence	41

3.2.4	Spatial coherence	42
3.2.5	Temporal coherence	43
3.3	A quantitative discussion of coherence	44
3.3.1	Coherence function	45
3.3.2	The relationship between the coherence function and fringe visibility	45
3.3.3	Van Cittert–Zernike theorem	46
3.4	Fluctuations in light waves	52
3.4.1	A statistical model for quasimonochromatic light	52
3.4.2	The second-order coherence function	55
3.4.3	Photon noise	56
3.4.4	Photodetectors	58
	<i>References</i>	62
4	Aperture synthesis	64
4.1	Aperture synthesis	64
4.1.1	The optics of aperture synthesis	64
4.1.2	Sampling the (u, v) plane	66
4.1.3	The optimal geometry of multiple telescope arrangements	69
4.2	From data to image: the phase problem	71
4.2.1	Phase closure	73
4.3	Image restoration and the crowding limitation	75
4.3.1	Algorithmic image restoration methods	76
4.3.2	The crowding limitation	77
4.4	Signal detection for aperture synthesis	78
4.4.1	Wave mixing and heterodyne recording	78
4.5	A quantum interpretation of aperture synthesis	81
4.6	A lecture demonstration of aperture synthesis	83
	<i>References</i>	87
5	Optical effects of the atmosphere	88
5.1	Introduction	88
5.2	A qualitative description of optical effects of the atmosphere	90
5.3	Quantitative measures of the atmospheric aberrations	93
5.3.1	Kolmogorov's (1941) description of turbulence	93
5.3.2	Parameters describing the optical effects of turbulence: Correlation and structure functions, $B(r)$ and $D(r)$.	95
5.4	Phase fluctuations in a wave propagating through the atmosphere	96
5.4.1	Fried's parameter r_0 describes the size of the atmospheric correlation region	99

5.4.2	Correlation between phase fluctuations in waves with different angles of incidence: the isoplanatic patch	100
5.5	Temporal fluctuations	102
5.5.1	The wind-driven “frozen turbulence” hypothesis	102
5.5.2	Frequency spectrum of fluctuations	102
5.5.3	Intensity fluctuations: twinkling	103
5.6	Dependence on Height	108
5.7	Dependence of atmospheric effects on the wavelength	108
5.8	Adaptive optics	109
5.8.1	Measuring the wavefront distortion	111
5.8.2	Deformable mirrors	113
5.8.3	Tip-tilt correction	114
5.8.4	Guide stars	114
5.9	Short exposure images: speckle patterns	115
5.9.1	A model for a speckle image	116
	<i>References</i>	119
6	Single-aperture techniques	120
6.1	Introduction	120
6.2	Masking the aperture of a large telescope	123
6.3	Using the whole aperture: speckle interferometry	126
6.3.1	Theory of speckle interferometry	128
6.3.2	Experimental speckle interferometry	130
6.3.3	Some early results of speckle interferometry	133
6.4	Speckle imaging	134
6.4.1	The Knox-Thompson algorithm	135
6.4.2	Speckle masking, or triple correlation	136
6.4.3	Spectral speckle masking	139
	<i>References</i>	139
7	Intensity interferometry	141
7.1	Introduction	141
7.2	Intensity fluctuations and the second-order coherence function	142
7.2.1	The classical wave interpretation	142
7.2.2	The quantum interpretation	146
7.3	Estimating the sensitivity of fluctuation correlations	147
7.4	The Narrabri intensity interferometer	149
7.4.1	The electronic correlator	150
7.5	Data analysis	152
7.5.1	Double stars	152
7.5.2	Stellar diameters	154

7.5.3	Limb darkening	154
7.6	Astronomical results	154
7.7	Retrieving the phase	155
7.8	Conclusion	156
	<i>References</i>	157
8	Amplitude interferometry: techniques and instruments	158
8.1	Introduction	158
8.1.1	The Michelson stellar interferometer	159
8.1.2	The Narrabri Intensity Interferometer	160
8.1.3	Aperture masking	161
8.2	What do we demand of an interferometer?	161
8.3	The components of modern amplitude interferometers	162
8.3.1	Subapertures and telescopes	163
8.3.2	Beam lines and their dispersion correction	165
8.3.3	Correction of angular dispersion	167
8.3.4	Path-length equalizers or delay lines	168
8.3.5	Beam-reducing optics	170
8.3.6	Beam combiners	170
8.3.7	Semireflective beam-combiners	172
8.3.8	Optical fiber and integrated optical beam-combiners	174
8.3.9	Star tracking and tip-tilt correction	175
8.3.10	Fringe dispersion and tracking	179
8.3.11	Estimating the fringe parameters	180
8.3.12	Techniques for measuring in the photon-starved region	183
8.4	Modern interferometers with two subapertures	184
8.4.1	Heterodyne interferometers	185
8.4.2	Interféromètre à 2 Télescopes (I2T)	186
8.4.3	Grand interféromètre à deux télescopes (GI2T)	186
8.4.4	The Mark III Interferometer	189
8.4.5	Sydney University stellar interferometer (SUSI)	189
8.4.6	The large binocular telescope (LBT)	191
8.4.7	The Mikata optical and infrared array (MIRA-I.2)	193
8.4.8	Palomar testbed interferometer (PTI)	193
8.4.9	Keck interferometer	196
8.5	Interferometers with more than two subapertures	197
8.5.1	The Cambridge optical aperture synthesis telescope (COAST)	197
8.5.2	Center for High Angular Resolution Astronomy (CHARA)	200
8.5.3	Infrared optical telescope array (IOTA)	202

8.5.4	Navy prototype optical interferometer (NPOI)	203
8.5.5	The Berkeley infrared spatial interferometer (ISI)	205
8.5.6	Very large telescope interferometer (VLTI)	208
	<i>References</i>	210
9	The hypertelescope	212
9.1	Imaging with very high resolution using multimirror telescopes	212
9.2	The physical optics of pupil densification	214
9.2.1	A random array of apertures	214
9.2.2	A periodic array of apertures	219
9.3	The field of view of a hypertelescope and the crowding limitation	221
9.4	Hypertelescope architectures	224
9.4.1	Michelson's stellar interferometer as a hypertelescope, and multi-aperture extensions	224
9.4.2	Hypertelescope versions of multitelescope interferometers	224
9.4.3	Carlina hypertelescopes	224
9.4.4	A fiber-optical version of the hypertelescope	226
9.5	Experiments on a hypertelescope system	228
	<i>References</i>	231
10	Nulling and coronagraphy	232
10.1	Searching for extrasolar planets and life	232
10.2	Planet detection methods	233
10.2.1	The relative luminosities of a star and planet	234
10.2.2	Requirements for imaging planet surface features	235
10.3	Apodization	236
10.3.1	Apodization using binary masks	238
10.3.2	Apodization using phase masks	239
10.4	Nulling methods in interferometers	240
10.4.1	Bracewell's single-pixel nulling in nonimaging interferometers	241
10.4.2	Bracewell nulling in imaging interferometers	242
10.4.3	Achromatic nulling in Bracewell interferometers	243
10.4.4	Starlight leakage in nulling interferometers	245
10.5	Imaging coronagraphy	247
10.5.1	The Lyot coronagraph in its original and stellar versions	248
10.5.2	The Roddier–Roddier phase-dot coronagraph	251
10.5.3	Four-quadrant phase-mask and phase-spiral coronagraphs	251
10.5.4	The achromatic interference coronagraph	252
10.5.5	Elementary modeling of mask coronagraphs	252

10.5.6	Mirror bumpiness tolerance calculated with Maréchal's equation	253
10.6	High contrast coronagraphy and apodization	256
10.6.1	Adaptive coherent correction of mirror bumpiness	256
10.6.2	Adaptive hologram within the coronagraph	257
10.6.3	Incoherent cleaning of recorded images	259
10.6.4	Comparison of coherent and incoherent cleaning	259
	<i>References</i>	260
11	A sampling of interferometric science	262
11.1	Interferometric science	262
11.2	Stellar measurements and imaging	262
11.2.1	Stellar diameters and limb darkening	262
11.2.2	Star-spots, hot spots	265
11.2.3	Pulsating stars	266
11.2.4	Miras	267
11.2.5	Young stellar object disks and jets	268
11.2.6	Dust shells, Wolf–Rayets	268
11.2.7	Binary stars	270
11.3	Galactic and extragalactic sources	271
11.3.1	SN1987a	271
11.3.2	R136a	272
11.3.3	The galactic center	273
11.3.4	Astrometry	273
11.4	Solar system	274
11.4.1	The Galilean satellites	274
11.4.2	Asteroid imaging	274
11.4.3	Pluto–Charon	275
11.5	Brown dwarfs	275
11.6	Solar feature imaging and dynamics measurements	275
	<i>References</i>	276
12	Future ground and space projects	278
12.1	Future ground-based projects	278
12.1.1	New ground-based long-baseline interferometers	279
12.1.2	The optical very large array (OVLA)	280
12.1.3	Toward large Carlina hypertelescopes	281
12.1.4	Comparison of OVLA and Carlina concepts	281
12.1.5	Comparing compact and exploded ELTs	282
12.1.6	Coupling telescopes through fibers: the OHANA project at Mauna Kea	283

12.2	Future space projects	284
12.2.1	Flotillas of mirrors	285
12.2.2	Darwin	285
12.2.3	Terrestrial planet finder (TPF)	287
12.2.4	Space interferometry mission (SIM)	288
12.2.5	The exo-Earth imager (EEI)	289
12.3	Simulated Exo-Earth-Imager images	290
12.3.1	Some speculations on identifying life from colored patches	291
12.4	Extreme baselines for a Neutron Star Imager	292
	<i>References</i>	294
	Appendix A	295
A.1	Electromagnetic waves: a summary	295
A.1.1	Plane and spherical electromagnetic waves	296
A.1.2	Energy and momentum in waves	297
A.2	Geometrical phase in wave propagation	298
A.3	Fourier theory	300
A.3.1	The Fourier transform	301
A.3.2	Some simple examples	302
A.3.3	Convolution	305
A.3.4	Sampling and aliasing	307
A.4	Fraunhofer diffraction	311
A.4.1	Random objects and their diffraction patterns: speckle images	313
	Appendix B	316
	<i>References</i>	317
	<i>Index</i>	319

Illustrations

Antoine Labeyrie and Stephen Lipson Peter Nisenson	<i>page</i> xxix xxxii
1.1 Mask used by Stéphane on the Marseilles telescope. This mask provides a pair of identical apertures with the largest separation possible.	3
1.2 Michelson's 20-foot beam stellar interferometer. (a) Optical diagram; (b) a photograph of the instrument, as it is today in the Mount Wilson Museum (reproduced by permission of the Huntington Library).	5
2.1 Young's fringes between light passing through two pinholes separated vertically: (a) from a monochromatic source; (b) from a polychromatic line source; (c) from a broad-band source.	10
2.2 Template for preparing your own double slit. Photocopy this diagram onto a viewgraph transparency at 30% of full size, to give a slit spacing of about 1 mm.	11
2.3 A typical observation of an urban night scene photographed through a pair of slits separated vertically by about 1 mm. Approximate distances to the street lights are shown on the right.	12
2.4 Waves on a still pond, photographed at (a) $t = 0$, (b) $t = 2$ and (c) $t = 4$ sec. The radius r of a selected wavefront, measured from the source point, is shown on each of the pictures.	13
2.5 Huygens, principle applied to (a) propagation of a plane wave, (b) propagation of a spherical wave, (c) diffraction after passage through an aperture mask.	16
2.6 Huygens' principle applied to gravitational lensing. (a) The distortion of the wavefront of a plane wave in the region of a massive body, causing a dimple on the axis, propagation of the dimpled wavefront, and the way in which multiple images result; (b) an example of the gravitationally distorted image of a quasar in the near infrared (courtesy of NASA).	17
2.7 Speckle pattern amplitude resulting from the superposition of 17 real-valued plane waves with random phases traveling in random directions. Black is most negative and white most positive.	19
2.8 Simulation of the development of an image out of noise as the number of photons in each white pixel increases.	21

- 3.1 The Michelson interferometer: (a) optical layout; (b) a typical fringe pattern from an extended source, when the configuration of figure 3.2 (b) is used. 25
- 3.2 The two virtual images I_{2B} and I_{B1} of a source point S as seen through the mirrors M_1 , M_2 and beam-splitter BS of a Michelson interferometer. Image I_{2B} , for example, is formed by reflecting S first in M_2 , giving image I_2 , and then reflecting I_2 in BS . The fringe patterns result from the interference between the two virtual images. In (a) the two images are side-by-side, and equidistantly spaced straight fringes are seen; in (b) they are one behind the other, and the concentric ring interference pattern is like figure 3.1(b). 27
- 3.3 Fraunhofer diffraction by an aperture, using Huygens' principle. When $|x| < H \ll L$, ϕ is small and $OQ - PQ = OT \approx x \sin \theta$. 29
- 3.4 Three experimental arrangements for observing Fraunhofer diffraction patterns: (a) with an expanded laser beam illuminating the mask, and a converging lens which gives the diffraction pattern in its focal plane; (b) visually, viewing a distant point source of monochromatic light and putting the mask directly in front of the eye pupil; (c) a point star observed by a telescope, where the mask is the telescope aperture. 30
- 3.5 The Fraunhofer diffraction pattern of a pair of slits each having width $2b$ separated by $2a$ when $a = 6b$: (a) amplitude; (b) intensity; (c) amplitude when there is a phase difference $2\Delta = 1$ rad between the slits. 33
- 3.6 The diffraction pattern of a square aperture: (a) the calculated pattern, $[\text{sinc}(ua)\text{sinc}(va)]^2$; (b) an experimental observation. In both cases the central region has been "over-saturated" so as to emphasize the secondary peaks. 34
- 3.7 Description of a limited periodic array of finite apertures by means of multiplication and convolution. (a) Two infinite vectors of δ -functions at angles 0 and γ are convolved to give a two-dimensional array of δ -functions. (b) This is multiplied by the bounding-aperture function $c(\mathbf{r})$ (a circle). (c) The resulting finite array of δ -functions is convolved with the individual aperture $g(\mathbf{r})$. 35
- 3.8 Schematic description of the transform of the array in figure 3.7. The individual transforms of the vector of δ -functions, $c(\mathbf{r})$ and $g(\mathbf{r})$; then (a), (b) and (c) are the transforms of the corresponding processes in that figure. 36
- 3.9 (a) A finite array of apertures and (b) its diffraction pattern. 36
- 3.10 The diffraction pattern of a circular aperture: (a) the calculated pattern, $[2\pi R^2 J_1(\rho R)/\rho R]^2$; (b) an experimental observation. In both cases the central region has been "over-saturated" so as to emphasize the rings. 38
- 3.11 The diffraction pattern of an annular aperture: (a) the calculated pattern $[\pi R t J_0(\rho R)]^2$, on the same scale as that of figure 3.10; (b) an experimental observation. 39
- 3.12 Showing the relationship between the autocorrelation function (overlap area between the aperture and itself, shifted by R) and the optical

- transfer function. The spatial frequency is related to R by $u = R/f\lambda$, where f is the focal length, in the paraxial approximation. 40
- 3.13 The phase difference between the waves from a point source Q reaching the pinholes A and B depends on their separation r . Drawing A' such that $QA = QA'$, the phase difference is seen to be $k_0BA' \approx k_0r\alpha$ for small α . On the screen, the zero-order fringe is at P , where QP passes through the mid-point of the two pinholes. The fringes from O and Q as shown have π phase difference, so that r is about equal to r_c . 42
- 3.14 A schematic picture of the coherence region; interference can be observed between points separated in space and time by a vector lying within this region. 44
- 3.15 Fringes observed between sources with degrees of coherence (a) $\gamma = 0.97$, (b) 0.50 and (c) -0.07 . Notice in (c) that there is minimum intensity on the center line, indicating that $\Delta = \pi$. 47
- 3.16 Direction cosines (ℓ, m, n) of a vector. The components ℓ, m and n are the cosines of the angles shown as L, M and N . 48
- 3.17 Geometry of the proof of the Van Cittert–Zernike theorem. 48
- 3.18 Phase and value of the coherence function $\gamma(w)$ for a circular star of angular diameter $\alpha = 10^{-3}$ arcsec. 50
- 3.19 Coherence function for limb-darkened circular disks. (a) shows $\gamma(r)$ for three degrees of limb-darkening, and (b) shows the same data when scaled so that the first zeros of the three curves coincide. 51
- 3.20 Value and phase of the coherence function $\gamma(u, v)$ for a pair of disk-like stars with angular diameter 0.5 mas, separated by 1.5 mas and with intensity ratio $1:2$. (a) shows $|\gamma(u, v)|$ as a contour plot with contours at $0.05, 0.1, 0.2, 0.4, 0.6$, and 0.8 . (b) shows $\cos \Delta$ in gray scale ($1 = \text{white}$ to $-1 = \text{black}$); in both figures u and v are in units of $10^8\lambda$. 52
- 3.21 Image of the double star Capella, obtained by the COAST group in 1997 at $1.29 \mu\text{m}$ (Young 1999). The circle at $(-100, -100)$ indicates the resolution limit. 53
- 3.22 Incoherent waves simulated by adding 20 components with unit amplitude and randomly chosen frequencies within the band $\omega_0 \pm \delta\omega$. (a) $\omega/\delta\omega_0 = 6$; (b) $\omega/\delta\omega_0 = 16$. In both cases the phase, relative to the phase at the start of the example, and the amplitude measured during periods T_0 are shown. The coherence time $\tau_c = (\delta\omega)^{-1}$ is the length of a typical wave group. 55
- 3.23 The intensity coherence function $\gamma^{(2)}(\tau)$ for a partially coherent wave with Gaussian profile and linewidth $\delta\omega = \tau_c^{-1}$. 56
- 3.24 Super-Poisson statistics. (a) Typical intensity fluctuations in a wave, generated as in figure 3.22; (b) corresponding photo-electron sequence; (c) photo-electron sequence for a steady wave with the same mean intensity as (a). 58
- 4.1 The (u, v) plane and time-difference compensation. 65
- 4.2 Geometry of aperture synthesis. 66

- 4.3 Synthetic point spread functions for a polar star: (a) single baseline B compared to (b) the optical point spread function for a circular aperture of diameter B and (c) sum of baselines $0.5B$, $0.75B$ and B with equal weights. 67
- 4.4 Two examples of (u, v) plane coverage (arbitrary units) and calculated equally-weighted point spread functions for a group of three receivers observing sources (a) on the Earth's axis and (b) at 6° to the equator. The receivers are arranged in a 3-4-5 triangle with the 4-unit side EW, situated at latitude 60° . 68
- 4.5 Annular and "Y" receiver arrays, and the corresponding autocorrelation functions. (a) A circular array of five receivers and (b) its autocorrelation function; (c) five receivers in a "Y" array and (d) their autocorrelation. The black circles A to E represent receiver positions and the open circles peaks in the autocorrelation function. The lines represent the construction vectors. 70
- 4.6 The Reuleaux triangle. 71
- 4.7 Autocorrelation functions for 24 receivers around a Reuleaux triangle: (a) on the triangle, but spaced non-uniformly around it; (b) with deviations from the triangle to optimize autocorrelation uniformity. The triangles show the receiver positions, and the dots the autocorrelation points. From Keto (1997). 72
- 4.8 (a) A nonredundant array of four receivers; (b) a redundant array, in which vectors 13 and 34 are equal. 74
- 4.9 Normalized fringe visibilities and phases determined by phase closure for Capella at 830 nm (Baldwin et al. 1996). 76
- 4.10 Illustrating the principle of heterodyne detection: (a) the signal, as a function of time; (b) the local oscillator; (c) the square of the sum of the amplitudes of (a) and (b), which is the instantaneous intensity measured by the detector; (d), (e) and (f) the detector output after filtering through a filter which passes frequencies between f_{\min} and f_{\max} ((d) – real part, (e) – imaginary part and (f) – modulus). The filtering is illustrated in figure 4.11. The observer is interested in the envelope of the signal (a), which is retrieved in (f); its phase can also be found from (d) and (e). 80
- 4.11 The spectra of the wave (c) in figure 4.10, (a) before, and (b) after filtering through the band-pass filter window shown. Note that the signal shown contains two basic frequencies, so that the sum and difference spectra each contain two peaks. Fourier synthesis based on the filtered spectrum (b) returns the demodulated signals (d), (e) and (f) in figure 4.10. 81
- 4.12 An experiment in which two lasers interfere, and four output signals are obtained. BS is a beam-splitter and D is a detector. The individual signals from detectors D_1 to D_4 consist of randomly arriving photons and contain no signs of the interference (i.e. dependence on the phase shifter P) but correlation between the signals shows the expected sinusoidal dependence on the phase. 83

4.13	Demonstration of aperture synthesis: (a) the optical bench layout; (b) stationary fringe pattern with a single “star” and two holes in the rotating mask; (c) as (b), but with a double star.	84
4.14	In (a) and (b) we see integrated images when the mask rotates, corresponding to figure 4.13(b) and (c). Deconvolution of (b) using (a) as the point spread function gives the “clean” image (c).	85
4.15	Mask holder to simulate diurnal rotation of two antennas at different latitudes observing a non-polar star.	86
5.1	Image of a point star through a 5-m telescope with an exposure of a few ms.	89
5.2	Laboratory image of a point source through a polyethylene sheet.	89
5.3	Typical height profile of atmospheric turbulence.	91
5.4	Effects of inhomogeneous refractive index on light rays.	92
5.5	Schematic diagram of the structure function $D_n(r)$. A typical value of C_{n^2} is $10^{-17} \text{ m}^{-\frac{2}{3}}$.	96
5.6	Power spectrum for phase fluctuations, measured interferometrically using a 1 m baseline at $\lambda = 633 \text{ nm}$ (Nightingale and Buscher 1991). The two lines show $f^{-\frac{2}{3}}$ and $f^{-\frac{8}{3}}$ at low and high frequencies, respectively.	104
5.7	The function $h^\mu C_n^2(h)$ indicating the relative importance of turbulence at different heights in determining (a) the phase correlations ($\mu = 0$), (b) the size of the isoplanatic patch ($\mu = \frac{5}{3}$), (c) scintillations for a small telescope ($\mu = \frac{5}{6}$), (d) scintillations averaged by a large telescope ($\mu = 2$).	107
5.8	Schematic diagram of a telescope with adaptive optical correction, operating with negative feedback.	111
5.9	Hartman–Shack wavefront distortion sensor. The deviation of each focus is proportional to the local wavefront slope.	112
5.10	Deformable mirrors of different types: (a) monolithic piezoelectric block, (b) discrete piezoelectric stacks, (c) bimorph mirror, (d) electrostatically deformed membrane (courtesy E. Ribak).	113
5.11	Simulated speckle images, using the structure function (5.28), with $r_0 = 7$ units. (a) The phase field across a circular aperture, radius 64 units. Phase, modulo 2π , is indicated by gray level from white to black. (b) The point spread function corresponding to the phase field (a). (c) The ideal point spread function for the same circular aperture. (d) Long-exposure average of 50 random simulations like (b).	116
5.12	More simulated speckle images, as in figure 5.11. (a) When the range of the phase fluctuations is less than 2π , a strong spot develops at the center. The range here is 1.95π which is close enough to 2π to allow both the speckle image and the strong spot to be seen at the same time; otherwise the image looks the same as figure 5.11(c). (b) The shape of each individual speckle is approximately a diffraction limited point spread function; in this case a small square aperture was used. (c) and (d) Single-slit and double-slit apertures. For the double-aperture telescope, each speckle is crossed by Young’s fringes.	118
6.1	Fringes due to two small ($< r_0$) circular holes in a mask, with an arbitrary phase difference and partial coherence ($\gamma \sim 0.3$) between them.	124

- 6.2 Fringes due to three small circular holes in a mask, each with an arbitrary phase and each pair having a different separation: (a) mask, (b) the diffraction pattern and (c) the transform of the measured diffraction pattern (autocorrelation function). 124
- 6.3 Nonredundant aperture mask used by Tuthill et al. (2000a) on the 10-m Keck multimirror telescope. 126
- 6.4 Four high-resolution image reconstructions of IRC+10216 at $2.2 \mu\text{m}$ on different dates (Tuthill et al. 2000b). 127
- 6.5 Reconstructions of WR-104 with all phases assumed zero or π , and with phases deduced by phase closure (Monnier 2000). 127
- 6.6 Speckle images (above) and corresponding spatial power spectra (below). From left to right, Betelgeuse (resolved disk), Capella (resolved binary) and an unresolved reference star. The scales are r/F which are angular stellar coordinates (the bar shows 1 arcsec) and correspondingly uF which are reciprocal angular coordinates (the bar shows 50 arcsec^{-1}). The power spectra are each the sums of about 250 frames (Labeyrie 1970). 129
- 6.7 Optics originally used by Labeyrie, Stachnik and Gezari for speckle interferometry. Atmospheric dispersion was compensated by translating the TV camera axially, the entire instrument being rotatable and oriented so that the grating dispersion was in the direction of the zenith. Analogue Fourier analysis of the recorded images used Fraunhofer diffraction. 130
- 6.8 Schematic diagram of a speckle camera with atmospheric dispersion corrector and band-limiting optical filter used at the Bernard Lyot telescope at Pic du Midi (Prieur et al. 1998). This speckle camera uses a PAPA detector. 130
- 6.9 A channel-plate image intensifier. 131
- 6.10 The PAPA camera. 133
- 6.11 A short-exposure speckle image of the double star Capella (α -Aur), in which each speckle can clearly be identified as a pair, separated along the diagonal. 135
- 6.12 A diffraction-limited image retrieved by triple-correlation, courtesy of G. Weigelt: (a) shows the long-exposure image of R136 in the 30 Doradus nebula; (b) a single short-exposure image; and (c) the reconstructed image of the source. The scale bars correspond to 1 arcsec. (Pehlemann et al. 1992). 136
- 6.13 The idea behind triple correlation, illustrated for a binary with unequal components. (a) shows the true image of the binary star and (b) the vector separating the two elements, as determined by speckle interferometry. (c) shows the atmospheric point spread function, i.e. the image of a point star. (d) is the convolution of (a) and (c), i.e. the speckle image observed. (e) shows the overlap of (d) with itself shifted by the vector (b), the product (f) being the retrieved speckle image of a point star, which should be compared with (c). (g) shows the correlation of (d) with (f), created by rotating (b) by 180° and centering

- it on each of the speckles of (f) successively. At its center, one image of (a) stands out above the noisy background. 138
- 7.1 A partially coherent wave simulated by superposing waves with random frequencies in a band of width 0.05 times the center frequency. (a) shows the wave amplitude, (b) the phase (compared with a pure sine wave at the center frequency) and (c) the fluctuating intensity of the wave. 143
- 7.2 Hanbury Brown and Twiss's experiments to show correlation between intensity fluctuations of two waves from the same source: (a) temporal correlation, as a function of the time delay z/c ; (b) spatial correlation, as a function of the lateral displacement r . PMT indicates a photomultiplier tube. 144
- 7.3 Results of Hanbury Brown and Twiss's second experiment (figure 7.2b) showing spatial correlation between intensity fluctuations in waves from a pinhole 0.19 mm diameter in Hg light $\lambda = 435.8$ nm. The curve shows the theoretical result (Hanbury Brown and Twiss 1956b). 145
- 7.4 Correlation between intensity fluctuations and individual photon events. (a) The intensity of the wave shown in figure 7.1. The mean intensity is shown by the broken line. (b) and (c) Two independent streams of photons generated randomly with probability at each time proportional to the intensity of (a) at that time. These have "super-Poisson" distributions. (d) A stream of photons generated randomly with probability proportional to the mean intensity of (a), showing a Poisson distribution. The three sequences (b)–(d) total the same number of events. (e) Coincidences between the photon events in (b) and (c) using time-slots narrower than the average interval between the photons in (d). The coincidences are almost nonexistent, which is why photon coincidence experiments failed to confirm the original intensity-correlation experiments. 147
- 7.5 Correlation measured for Sirius with baselines up to 9 m in 1956 (Hanbury Brown 1974). This can be compared with the later data in figure 7.9. 149
- 7.6 Layout of the Narrabri intensity interferometer. Notice that the baseline is always normal to the direction of the star, so that with equal-length cables, the signals arrive simultaneously at the correlator. 150
- 7.7 Schematic diagram of the correlator and integrator system (after Hanbury Brown 1974). 151
- 7.8 Correlation data measured for three stars, showing the dependence on their angular diameters (after Hanbury Brown 1974) 153
- 7.9 Correlation data measured at Narrabri for Sirius, showing in particular the second peak, whose height is critical in determining details of limb darkening (Hanbury Brown 1974). 155
- 8.1 The blocks, or subsystems, from which a stellar interferometer is composed. Extra optics for focusing, filtering, etc. may be inserted at any of the positions indicated by vertical double broken lines. 159

- 8.2 Michelson stellar interferometer, showing the path-length corrector and the tilt plate used to ensure overlap of the two images. 160
- 8.3 Cassegrain optics (a) as a telescope, (b) as a beam-compressor. In (a), the flat folding mirror could equivalently, although not in terms of cost, be a large mirror before the telescope, in which case the telescope is fixed in orientation. Otherwise, the telescope is pointed towards the star, and the small flat mirror is best located at the mechanical node where both axes of rotation intersect. The vertical axis of rotation does not coincide with the optical axis of the telescope, but intersects the horizontal one on the folding mirror. See also figure 8.4. 165
- 8.4 Example of the sequence of mirrors in one beam line at CHARA, designed in order to control polarization effects. Each beam line has the same number of mirrors reflecting at the same angles. 166
- 8.5 Dispersion correctors: (a) path-length and dispersion; (b) angular, using two Risley prism pairs. 167
- 8.6 (a) Typical design of a path equalizer, using a cat's-eye reflector. (b) shows the alternative corner-cube reflector. (c) Delay lines at CHARA. 169
- 8.7 Power spectrum of the mixed signals from three telescopes at COAST observing Vega in 1993. Each peak occurs at the difference frequency corresponding to a particular pair of telescopes. After Baldwin et al. (1994). 170
- 8.8 A Gregorian beam reducer for two parallel beams, with a common field stop in the real image plane (SUSI). 171
- 8.9 Two-beam combiner at SUSI for shorter visible wavelengths. Polarizing beam-splitters (PBS) are first used to extract one polarization for tip-tilt guidance by the quadrant detectors (QD) and the slits (S) are used for spectral selection. RQD is a reference quadrant detector. 172
- 8.10 Beam-combining optics designs for NPOI: (a) three inputs and three pairwise outputs; (b) six inputs and three outputs, each combining four of the inputs (NPOI). 173
- 8.11 A Sagnac interferometer used to create a square matrix of interference patterns between elements of an array of inputs: (a) optical design; (b) example of the observed matrix for a laboratory double star; note that symmetrically placed off-diagonal elements have similar contrasts. 174
- 8.12 Optical layout of the fiber-linked beam-combiner for the near infrared (FLUOR). 174
- 8.13 Integrated optic infrared beam-combiner for three inputs (IONIC). Photograph courtesy of Alain Delboulbe, LAOG. 175
- 8.14 Fringes at $\lambda = 1.65 \mu\text{m}$ between the pairs of three telescopes at IOTA obtained using the integrated-optics combiner shown in figure 8.13. Figure courtesy of P. Schuller, IOTA. 176
- 8.15 Star image slightly off-center on a quad cell. 177
- 8.16 One-dimensional point spread function ($\text{sinc } x$) with the masking function $\text{sign}(df/dx)$. (a) shows the PSF centered with respect to the mask, and (b) shows the situation after a small movement; the shaded regions indicate signals which contribute to the detected output, with

their signs indicated. All the positive signals are greater than the adjacent negative ones.	178
8.17 Polychromatic fringe groups with (a) $\lambda/\delta\lambda = 3$ and (b) $\lambda/\delta\lambda = 10$.	179
8.18 Two spectrally dispersed interferograms (wavelength range 2.0–2.4 μm) (a) path-length compensated; (b) with an error in path-length compensation (GI2T: Weigelt et al. 2000).	179
8.19 Light from two inputs 1 and 2 interferes at an ideal beam-splitter with an optional additional phase shift of $\pi/2$ and goes to two detectors A and B.	180
8.20 Plots of series of $M = 100$ observations as points in the $((n_1 - n_3), (n_2 - n_4))$ plane. (a) $N_0 = 8000, \gamma = 0.8$; (b) $N_0 = 8000, \gamma = 0.3$; (c) $N_0 = 80, \gamma = 0$; (d) $N_0 = 80, \gamma = 0.3$.	182
8.21 Measurement of spatial correlation of sunlight at 10 μm using heterodyne detection with a CO_2 laser local oscillator (Gay and Journet 1973).	185
8.22 I2T. In the drawing of the optical layout, M is a 250-mm primary mirror, m is a Cassegrain secondary, F a coudé flat, L a field lens, RM a roof mirror in the pupil plane, D a dichroic mirror, TV1 a guiding camera, BL a bilens to separate the two guiding images; S and P are slit and prism which can be inserted to observe dispersed fringes and TV2 a photon-counting camera with 500–700 nm filter.	187
8.23 Fringes observed on Vega with I2T.	188
8.24 GI2T.	188
8.25 Schematic optics of the Mark III interferometer. BB indicates the broad-band detector used for fringe tracking.	190
8.26 Schematic linear layout of SUSI.	190
8.27 LBT optics: (a) the binocular telescope; (b) detail of the beam-combining region.	192
8.28 The (u, v) plane coverage of LBT for one complete rotation: (a) u -section of the autocorrelation function; (b) grayscale representation.	192
8.29 Optical layout and beam-combination at MIRA-I.2.	193
8.30 Optical layout of PTI. The metrology system uses laser interferometry traversing the same optics as the star beams, returning from the corner-cube reflectors in the shadow of the Cassegrain secondaries (lower drawing).	194
8.31 Examples from PTI of five consecutive fringe trains containing groups from two stars (Lane and Muterspaugh 2004).	195
8.32 Layout of the telescope stations and optics laboratory of COAST.	198
8.33 The u, v coverage diagram at $\lambda = 1 \mu\text{m}$ for one configuration of COAST observing a source at declination 45° (Haniff et al. 2002).	199
8.34 The beam-combining optics of COAST. The four detectors each receive one-quarter of the light from each telescope.	199
8.35 Schematic layout of CHARA at the Mount Wilson Observatory. The longest baseline is S1-E1 = 331 m.	200
8.36 Simplified schematic optical layout for the fringe-tracking subsystem at CHARA, as if there were just four telescopes (in fact there are	

- seven). The CCDs record four (seven) superimposed fringe patterns, each with its own period. The reflections are shown to be at 90° ; in the real system these angles of reflection are much less, in order to minimize polarization problems. 201
- 8.37 Layout of the subaperture sites at IOTA. 202
- 8.38 Layout of the NPOI subaperture stations. The relative positions of the astrometric substations are measured by an independent laser metrology system which is not shown. 204
- 8.39 Synthesized images of the triple star η -Virginis on February 15 and May 19, 2002, after processing with CLEAN (section 4.3.1) (Hummel et al. 2003). 205
- 8.40 Layout of the eight ISI telescope sites at Mount Wilson. 207
- 8.41 Schematic flow diagram of the optical and RF signals in ISI. 208
- 8.42 (a) Layout of the VLT observatory, showing the four 8.2-m telescopes T1–T4 and 30 positions for 2-m auxiliary telescopes, joined by rail tracks. (b) and (c) show (u, v) -plane coverage for T1–T4 and three optimally chosen auxiliary telescopes, for source declinations of 0° and -35° , respectively. The u and v are in units of $10^6\lambda$. After von der Lühе et al. (1994). 209
- 9.1 A simulated raw image of an exo-Earth as would be recorded using a hypertelescope, with contrast enhancement. The aperture (a) has 150 subapertures equally spaced around three rings, the outermost one having diameter 150 km. The central peak and rings of the interference function (b) resemble the Airy pattern from a filled disk of identical outer size, but the outer rings are broken into speckles. (c) The simulated image of the Earth as seen from 10 light-years distance, using this hypertelescope. The central peak of (b) has been weakened by a factor of 4 in order to bring out the surroundings. 213
- 9.2 (a) A sparse array aperture. (b) A densified copy of (a) in which the pattern of subpupil centers is conserved with respect to the entrance pattern, while the size of the subpupils relative to their spacing is increased. (c) Densification achieved by the use of inverted Galilean telescopes. 214
- 9.3 Point spread function for 20 randomly spaced circular apertures of diameter D within a circle of radius $20D$. Notice the *interference function*, consisting of a sharp central point on a weaker speckle background, multiplied by the *diffraction function*, the coarser ring pattern which is the diffraction pattern of the individual apertures. 215
- 9.4 Densified pupil configuration using inverted (demagnifying) Galilean telescopes, and the composite wavefront formed: (a) normal incidence; (b) incidence at angle α . $g = 1.7$ in this figure. 216
- 9.5 Schematic profiles of undensified and densified images of a point source for a random array of apertures: (a) and (b): undensified, with object at angles 0 and α ; (c) and (d): densified, $g = 2$, with object at angles 0 and α . 219

- 9.6 (a) Aperture of a periodic array and (b) the reciprocal array of interference peaks in the point spread function. The scale of the latter is proportional to wavelength, so that if the source is polychromatic, the off-center peaks are dispersed into spectra. 220
- 9.7 The focal surface of a spherical mirror, with rays incident from two directions. The expanded view of the focal region indicates the geometrical origin of spherical aberration. 225
- 9.8 The principle of a Mertz (“clam-shell”) corrector, which compensates the difference between the sphere and paraboloid at a position close to the focus. Only one marginal and one paraxial ray are shown, but all intermediate rays focus to the same stigmatic image point. 225
- 9.9 Aerial view of the Arecibo radio telescope. 226
- 9.10 Hypertelescope concept using a balloon-supported coudé mirror and Merz corrector, and computer-controlled tethering. 227
- 9.11 Sequence of fringes observed on Vega during a 200 ms period with a two-subaperture hypertelescope. 227
- 9.12 (a) A fiber-coupled densifier and (b) a miniature hypertelescope due to Pedretti et al. (2000) using diffractive pupil densification. 228
- 9.13 Hypertelescope experimental set-up used in miniature form for preliminary testing. The incoming light beam from a Newtonian telescope is collimated by lens L_1 . A Fizeau mask installed for convenience in the pupil plane following L_1 , rather than at the primary mirror, has $N = 78$ holes of $100 \mu\text{m}$ size each. It defines in the entrance aperture a virtual “diluted giant mirror” of 10 cm size with 1 mm subapertures. The densification is achieved with two microlens arrays (ML_1 and ML_2). (Gillet et al. 2003). 229
- 9.14 (a) Image of Castor made using the miniature hypertelescope, showing the resolved binary A-B, spaced 3.8 arcsec. The half direct imaging field is about 14 ± 0.6 arcsec wide. (b) Image of Pollux, obtained with a 10-min exposure. It matches the theoretical pattern, with residual first orders due to incomplete pupil densification. With respect to the laboratory images and the numerical simulation, the peaks are however somewhat widened by seeing and exceed the theoretical arcsecond resolution limit of the 10-cm array.
(c) Numerical simulation of a monochromatic point source image with the 78-aperture hypertelescope. 229
- 9.15 A helium balloon supports the focal gondola in the focal sphere of an experimental hypertelescope (see figure 9.10). 230
- 10.1 Light flux spectra received from the Earth and Sun at a distance of 10 parsec. The ratio between the two graphs is independent of the distance. 235
- 10.2 An example of Slepian’s prolate function apodization mask (intensity attenuation factor as function of radius) and the cross-section of the point spread function, shown on a logarithmic scale. The abscissa angle θ is in units of λ/D , so that the first zero of the Airy function for the full aperture would be at 1.22 (Kasdin et al., 2003). 238

- 10.3 Nisenson and Papaliolios (2001) considered apodization of a square aperture with the sonine function $[(1 - x^2)(1 - y^2)]^3$. The figure shows diagonal cuts through the PSF in polychromatic light for a circular aperture, without apodization (1) and with sonine apodization (2), and a square aperture with sonine apodization (3) and with the addition of a planet of relative intensity 10^{-9} of the star (4). Abscissa angle θ as in figure 10.2. 238
- 10.4 Rotationally symmetric apodization mask providing an extended region of intensity below 10^{-10} : (a) the mask, (b) and (c) calculated PSF. Courtesy of R. J. Vanderbei. 240
- 10.5 Bracewell's concept of a Michelson interferometer with small subapertures used as a nulling interferometer. As a result of the phase shift, the waves from the two subapertures interfere destructively when the source is on the axis of the interferometer, but when the source is at a non-zero angle to the axis, constructive interference may be obtained. Because the requirements for nulling are less stringent in the infrared, this is practical in the mid-infrared region. 241
- 10.6 Nulling in an imaging interferometer. The picture sketches the sort of image expected, and the origin of starlight leakage. 243
- 10.7 An interferometer in which a π phase shift at the A exit is achieved using the Gouy effect. When an image is projected through this interferometer, the two interfering images at the exits are mutually rotated by 180° ; this effect is used in the achromatic interference coronagraph (section 10.5.4). 244
- 10.8 Electric field vectors before and after reflection at a perfectly conducting mirror. Note that there is a change in sense of rotation if the incident wave is circularly or elliptically polarized. 245
- 10.9 (a) An out-of-plane Michelson stellar interferometer in which an arbitrary phase shift 2α is achieved using the geometrical phase shift. (b) The route traced on the sphere of propagation vectors for the two waves in (a). 246
- 10.10 Sagnac-type interferometer creating π phase difference at the output (Tavrov et al. 2002). The two routes through the interferometer introduce geometric phases $\pm\pi/2$, respectively. 246
- 10.11 Fringe profiles using (a) two small subapertures with equal areas A_1 and phases 0 and π separated by B_1 ; (b) four small subapertures at positions $(0, 1, 2, 3)B_1$ with phases respectively $(\pi, 0, \pi, 0)$ and areas $(\frac{1}{3}A_1, A_1, A_1, \frac{1}{3}A_1)$. The maxima have been normalized to unity. In the subapertures, white indicates phase 0 and gray indicates π . 248
- 10.12 The Lyot coronagraph uses an opaque occulter disk in the focal image to mask the central Airy peak and a few rings in the diffraction pattern of the brighter source. A "Lyot stop" located in a pupil relayed by the field lens has an aperture slightly smaller than the geometric pupil. It masks the rings where light from the non-occulted Airy rings is mostly concentrated. In the image then relayed onto the camera C by

- the relay lens, the star's Airy pattern is strongly attenuated. The image of an off-axis planet is little affected. 249
- 10.13 Simulation of imaging a star and planet (intensity ratio 10^{-5}) by a Lyot coronagraph. (a) shows a magnified picture of the central "Airy disk" of the telescope image, and the dotted circle represents the edge of the occulter disk. (b) shows the same image after occulting, with contrast enhancement by 500 with respect to (a), so that the outer diffraction rings now become visible. (c) shows the re-imaged pupil, with the Lyot stop (dotted circle) and (d) the masked aperture pattern, with contrast enhancement 10 with respect to (c). The final coronagraph images (e) and (f), on a scale eight times smaller than (a) and (b), show the star respectively without and with the planet at the position indicated by the arrow. The intensity ratio between the planet and the star image in (f) is now about 0.2, an enhancement of 2×10^4 . 250
- 10.14 Detail of the ring in figure 10.13(c), showing its double structure. 250
- 10.15 Simulation of the four-quadrant phase mask coronagraph. The star and planet have intensity ratio 10^{-6} . The phase changes due to the mask are shown in (a). (b) shows the telescope image with the mask superimposed (magnified eight times with respect to (e) and (f)). This diffracts most starlight outside the relayed geometric pupil, shown in (c). (d) shows the field transmitted by the Lyot stop. (e) and (f) show, respectively, the final images without and with a planet along the diagonal. 251
- 10.16 Comparison of the images of planets with intensity 10^{-6} of their stars, as seen by the four-quadrant and phase-spiral coronagraphs when the planet is along a diagonal. The star image is off to the top left of the field of view. When the planet is close to the x or y axis, the background of the four-quadrant mask field (figure 10.15 e) is too high to discern such a weak planet. 252
- 10.17 Illustrating schematically the effect of coronagraphic field masks described as a superposition: (a) Lyot mask; (b) phase-dot mask. 253
- 10.18 (a–c) Simulated diffraction patterns of a circular aperture with wavefront degraded by different levels of wavefront bumpiness; (d–f) the same at the exit of an ideal coronagraph. The central peaks in (a–c) are overexposed in order to emphasize the surrounding speckle patterns. The coronagraph removes the theoretical Airy pattern of the aperture, and retains the contribution from the wave bumpiness. If the bumpiness is weak (d), this contribution is a centrosymmetrical speckle pattern, but not if the bumpiness is strong (f). There is no centro-symmetry in the speckles of (a–c) since the antisymmetric speckle phase interferes with the symmetric ring phase. 254
- 10.19 Lyot coronagraph containing hologram-like adaptive optics for nulling the residual star light. The focal occulter mask OM is a small optical wedge (inset) with pinhole PH, which deviates the main stellar light out of the imaging beam IB containing the planet's light, to provide a cleaned reference beam RB. Both beams, collimated and

- deviated by wedge lenses WL1 and WL2, intersect in the pupil plane, within the aperture of a Lyot stop LS. Their interference produces a hologram, recorded directly on a photosensitive plate or indirectly by a camera HC. The camera is fed by the beam-splitter BS and displays the recorded image as a phase pattern on the deformable plate DP which then behaves as a phase hologram. When it is transmitted through the hologram, the stellar wavefront in beam IB subtracts coherently from the copy of it reconstructed by the hologram as the first-order diffraction of the reference beam RB. The cleaned image of circumstellar features, including planets, is recorded by camera IC. 258
- 11.1 Visibility amplitude for α -Bootis at 905 nm measured at COAST. Notice the negative values determined by phase closure. The fit is to a limb-darkening model (Haniff et al. 2003). 263
- 11.2 Squared visibility amplitudes for ψ -Phe from VLTI. The right panel shows the second-lobe data expanded. Three models are shown: uniform disk (upper full line); fully darkened disk (lowest line) and a model atmosphere (center dashed line); (Wittkowski and Hummel 2003). 264
- 11.3 Image reconstruction of Betelgeuse in early 2004 in the TiO band at 782 nm, showing a hot spot (Haniff et al. 2004). 265
- 11.4 (a) Periodic variation of several parameters of δ -Cephei, after Carroll and Ostlie (1996). (b) Change of angular diameter of a Cepheid during one period of pulsation, measured at VLTI (Kervella et al. 2004). 266
- 11.5 Three epochs of the 2.2 μ m emission from WR 98a showing a rotating spiral structure. The white line indicates the best fit to a plume morphology (Monnier et al. 1999). 269
- 11.6 Maximum entropy images of NML Cyg showing the circumstellar environment. The scale bar is 100 mas. The left figure shows the image from non-redundant array imaging with the Keck I telescope, to which the IOTA data indicating an unresolved bright source has been added in the right-hand figure (Monnier et al. 2004). 270
- 11.7 Binary orbit of β -Centauri determined by SUSI (Davis et al. 2005). 271
- 11.8 Speckle interferometry observations of SN87a showing two ejected blobs (Nisenson and Papaliolios 1999). 272
- 12.1 Simulated image of a point source, formed by a coupled ELT and hypertelescope, having respectively a single 50-m mirror and 200 mirrors of 1-m diameter. The pupil densification is unequal, providing subpupils of equal size in the densified exit pupil. Left: the PSF of the 50-m telescope; right: that of the coupled system. The high-resolution interference peak thus obtained is seen to concentrate most energy, thus combining the advantages of both instruments. The sketch below shows the nonuniformly densified exit pupil where the 50-m and 1-m apertures appear with identical sizes. 279
- 12.2 The OVLA scheme originally proposed in the late 1970s involves tens of mobile telescopes, all feeding a common focus. The optical path lengths are kept balanced while the Earth rotates by moving the telescopes during the observation. They must remain on the elliptical

- locus, which is the intersection with the ground plane of a giant paraboloid kept pointed toward the star. 280
- 12.3 (a) Schematic layout of the telescopes on Mauna Kea which may eventually be linked in project OHANA. (b – d) Calculated instantaneous point spread functions at $2.0\ \mu\text{m}$ for an source at zenith for (b) the northern four telescopes, (c) the eastern three, (d) all the telescopes combined interferometrically. The first two baselines to operate will be Keck-I to Keck-II and Gemini to CFHT. 284
- 12.4 Darwin concept, using six telescopes which can move radially in a nulling configuration, and a central beam-combining spacecraft. (a) Spacecraft configuration. (b) Form of one individual nulling interferometer; the “area” a represents the relative wave amplitude (including its sign) from that aperture which is used in the interferometer. When three such interferometers are superimposed at 0 and $\pm 120^\circ$, the sum of the values of a^2 at each mirror is 9. (c) Fringe profile of one interferometer; the dashed line shows, for comparison, the form of $\sin^2 \theta$ fringes with the same fundamental period. 286
- 12.5 Darwin concept using three spacecraft in an equilateral triangle: (a) the optical paths from the three telescopes to the beam-combiner, each path being twice the length of one side of the triangle; (b) phasor combination for the three interfering waves for a source on axis; (c) phasor combination for an off-axis source which creates phase shifts $\pm\delta$ at the second and third inputs; (d) as (c), when the phases of the second and third beams are interchanged. 287
- 12.6 A rectangular apodization mask and its point spread function providing quadrant regions of intensity below 10^{-10} . Courtesy of R. J. Vanderbei. 288
- 12.7 Terrestrial Planet Finder-I. The optical scheme to create two independent nulling interferometers, which can be coherently combined. Four telescopes and a beam-combiner are situated on five satellites. 288
- 12.8 The Exo-Earth Imager concept in bubble form. This space version of a Carlina hypertelescope has a primary spherical locus M1 which is entirely, but sparsely, paved with mirrors. These can be fixed in space. Focal beam-combiners, each incorporating a clam-shell corrector which itself is a flotilla of small mirrors on loci M2 and M3 (inset), are movable on the half-radius focal sphere to acquire various stars. With many combiners, independently movable on the focal sphere, each primary mirror segment can feed several combiners simultaneously, thus increasing the observing efficiency. For a system of this size, all the elements can be plane mirrors. 289
- 12.9 Reflectance spectrum at normal incidence and an electron microgram of a synthetic opal. Courtesy of Z. V. Vardeny, University of Utah. 292
- 12.10 Beam-combination scheme for extreme baselines. A single large M2 concave mirror receives the Fizeau image at the common focus of the primary elements. It must capture most light from the star observed,

	and therefore must be larger than the central lobe of the Fizeau envelope. This defines the minimal sizes of mirrors at both ends. Several M3 mirrors receive the relayed subapertures and form a combined image at the entrance of the pupil densifier.	293
A.1	The wavevector \mathbf{k} , Poynting vector \mathbf{S} and electric and magnetic field vectors in a plane electromagnetic wave.	296
A.2	The Lorenz force between the wave's magnetic field and the current induced by its electric field results in light pressure on a conducting reflector.	298
A.3	Construction of a general \mathbf{k} -route on the surface of the sphere of wave-propagation directions.	300
A.4	Sketches of five simple one-dimensional functions $f(x)$ and their Fourier transforms $F(k)$. A Dirac δ -function is represented by a vertical arrow, and is assumed to have zero width and unit area.	304
A.5	Two-dimensional Fourier transforms: (a) a circular aperture; (b) an annular aperture.	306
A.6	Convolutions between one-dimensional functions: (a) one function is a set of δ -functions; (b) two rect functions with different widths.	306
A.7	Convolution between a two-dimensional array of δ -functions and a polygon.	307
A.8	(a) A function $s(t)$ with bandwidth much smaller than $2\pi/t_0$ sampled at intervals t_0 , its Fourier transform and the reconstruction from the cell of size $2\pi/t_0$. (b) The same when the bandwidth is close to $2\pi/t_0$ giving a poor reconstruction of $s(t)$. Note that the vertical arrows represent δ -functions, and the ordinate axis has been omitted to avoid confusion.	309
A.9	(a) A periodic function correctly sampled, its spectrum and reconstruction from the spectrum in the unit cell $2\pi/t_0$. (b) The same when the periodic signal is undersampled, showing the aliased signal reconstructed from the unit cell. Note that the vertical arrows represent δ -functions, and the ordinate axis has been omitted to avoid confusion.	310
A.10	Moiré fringes between overlaid grids with similar spatial frequencies.	310
A.11	Geometry for Fraunhofer diffraction by a two-dimensional mask in the plane $z = 0$.	312
A.12	(a) An aperture is repeated at random positions within a square region. (b) Experimental diffraction pattern $ G(u) ^2$ of one element of the array. (c) Diffraction pattern of the complete array in (a). The circular central region of the pattern was photographically underexposed in order to make the bright spot at the origin visible. From Lipson et al. (1995).	314

Preface

Although the optical telescope is the most venerated instrument in astronomy, it developed relatively little between the time of Galileo and Newton and the beginning of the twentieth century. In contrast to the microscope, which enjoyed considerable conceptual development during the same period from the application of physical optics, telescopes suffered from atmospheric disturbances, and therefore physical optics was considered irrelevant to their design. The realization that wave interference could be employed to overcome the atmospheric resolution limit was first recorded by Fizeau and put into practice by Michelson around 1900, but his experience then lay dormant until the 1950s. Since then, first in radio astronomy and later in optical and infrared astronomy, interferometric methods have improved in leaps and bounds. Today, many optical interferometric observatories around the world are adding daily to our knowledge about the cosmos.

The aim of this book is to build on a basic knowledge of physical optics to describe the ideas behind the various interferometric techniques, the way in which they are being put into practice in the visible and the infrared regions of the spectrum, and how they can be projected into the future. Some techniques consist of optical additions to existing large telescopes; others require complete observatories which have been built specially for interferometry. Today all these are being used to make accurate measurements of stellar angular positions, to discern features on stellar surfaces and to study the structure of clusters and galaxies. Tomorrow, maybe they will be able to image planetary systems other than our own. To this end, many new ideas are being generated and tested with the eventual aim of looking at an extrasolar Earth-like planet, either from the ground or from a space platform.

The book contains some introductory chapters on basic optics, which establish an unsophisticated physical and mathematical framework which is used to discuss the various ideas and instruments presented in the later chapters. It is hoped that, despite the inevitable use of mathematics, the physical principles of the astronomical interferometric techniques in the following chapters will be clear. In the final



Antoine Labeyrie and Stephen Lipson

chapters, some astrophysical results achieved by interferometry are discussed, and some untested future ideas are presented. The level of detail is hopefully sufficient for senior undergraduate and graduate students who are interested in understanding the ideas and implementations of astronomical interferometry. We have attempted to give fair credit to all those whose work has substantially advanced the field, without overloading the book with references to every detail.

Peter Nisenson first conceived of this book in 2002, and asked us to join him in writing it. Sadly, he never lived to see its publication, but he was active in determining its layout and he wrote fairly complete drafts of two chapters. As a result of this, we decided to continue the work as a memorial to his life-long dedication to astronomy, although his further contributions are sorely missing.

Many people have helped us in collecting and understanding the material presented, and have spent time showing us round their interferometric observatories. SGL wishes in particular to thank Dr Erez Ribak, from whom he has learnt such a lot through innumerable discussions on optics and astronomical interferometry. He is also grateful to Mark Colavita, Amir Giveon, David Snyder Hale, Chris Haniff, Pierre Kern, Nachman Lupu and Nils Turner for their time, help and comments. AL

wishes to thank the late Prof. André Lallemand and Pierre Charvin for their early support. Emile Blum, James Lequeux, Françoise Praderie and Arthur Vaughan gave crucial encouragement and Deane Peterson also encouraged, in the critical early stages, part of the work described in the book.

In addition, we should like to thank Laurent Koechlin, John Davis, Chris Haniff, Chris Dainty, Andrew Booth and Noam Soker, who have read and made useful comments on parts of the manuscript. Itzik Klein carried out the experiments described in section 4.6 and Carni Lipson drew some of the figures. We are also grateful to the many authors and journals for permission to reproduce figures and data, as indicated in the figure captions. SGL wishes to acknowledge the support of the Norman and Helen Asher Space Science Institute at Technion, and the hospitality of the Kavli Institute for Theoretical Physics, UCSB, where part of the manuscript was researched and written.

We should also like to thank our wives and families for their understanding during the periods when we have been necessarily absorbed in research and writing.

Antoine Labeyrie

Stephen Lipson

Plateau de Calern, August 2005.

Peter Nisenson, 1941–2004

This book was Peter Nisenson's idea. Peter received his BS degree from Bard University in New York, and continued with post-graduate work in Physics and Optics at Boston University. He was then employed as an optical scientist by the Itek Corporation in Lexington, MA, where he worked for 14 years. Both of us first met him there in 1973. At that time he was working on a programmable optical memory device (the PROM) which used a photoconducting crystal as a recording medium. When he first heard about speckle interferometry, he realized that this device could carry out the required Fourier transform on-line and therefore provide directly the image power spectrum. The three of us then met for the first time; an observing plan was proposed, supported by Itek, and carried out at Kitt Peak in December 1973. Although this particular project was not successful, it was probably the turning point in Pete's life, at which he decided to become a professional astronomer. In the same period, under the leadership of John Hardy with whom he had a life-long friendship, his group at Itek became heavily involved in adaptive optics, an involvement which led to his making some important measurements of atmospheric optical properties.

Pete was for five years a Research Associate at the Center for Earth and Planetary Physics at Harvard before joining the Harvard Smithsonian (CfA) in 1982, where he remained for 22 years. He worked on various exciting and innovative projects including the development of programs for high-resolution image reconstruction of solar and other astrophysical data, using speckle interferometry. Together with Costas Papaliolios and Steven Ebstein he developed the "Precision Analog Photon Address" (PAPA) image detector, which gave the digital addresses of individual photon events, one of a new generation of image detectors for astronomy, and which he used extensively for speckle interferometry.

He highlighted the use of interferometry during observations in Chile of the Supernova SN1987a, which received television prominence, as well as several



Peter Nisenson

publications. He then became involved in the extrasolar planet search, and contributed greatly to the creation and successful use of the “Advanced Fiber Optic Echelle” (AFOE) spectrograph, a technique that has been successfully used in recent years to discover several planets outside of our solar system. In addition he developed original concepts for imaging extrasolar planets using high-dynamical-range apodization techniques. He possessed a commanding knowledge of optics and his ability to envisage alternative ways to achieve a goal was invaluable to many projects.

During his period at CfA he became involved with the IOTA interferometer. In 2002 he originated the idea of writing a textbook about optical interferometric astronomy, with the feeling that this was becoming a mature technique and was already beginning to provide important astrophysical data. This book is the result, and is dedicated to his memory.

As a young man, Peter chose the study of math and physics over becoming a professional cello player but continued a life-long love of music. He was an avid

golf and tennis player and an active member of the Harvard College Observatory Tennis Club for years. Somewhat of a terror on the tennis court, he nevertheless delighted in encouraging others amongst his colleagues to join in the game, and the HCO Tennis Clinic has been named in his memory. Peter had been in poor health for the last year of his life, but throughout this time he stayed as active as his condition allowed him to be. He was survived by his wife Sarah (Sally), his son Kyle and his daughter Elizabeth.

1

Introduction

1.1 Historical introduction

The Earth orbits a star, the Sun, at a distance of 140 million km, and the distance to the next closest star, α -Centauri, is more than $4 \cdot 10^{13}$ km. The Sun is one star in our galaxy, the Milky Way. The Milky Way has 10^{11} stars and the distance from the Sun to its center is $2.5 \cdot 10^{17}$ km; it is one galaxy in a large group of galaxies, called the Local Group and the distance to the next nearest group, called the Virgo Cluster, is about $5 \cdot 10^{20}$ km. The Universe is made up of a vast number of clusters and superclusters, stretching off into the void for enormous distances. How can we learn anything about what's out there, and how can we understand its nature?

We can't expect to learn anything about distant galaxies, black holes or quasars, or even the nearest stars by traveling to them. We can maybe explore our own solar system but, for the foreseeable future, we will learn about the Universe by using telescopes, on the ground and in space.

The principal methods of astronomy are spectroscopy and imaging. Spectroscopy measures the colors of light detected from distant objects. The strengths and wavelengths of spectral features tell us how an object is moving and what is its composition. Imaging tells us what an object looks like. Because distant stars are so faint, the critical characteristic of a telescope used for spectroscopy is its light-gathering power and this is determined principally by its size, or "collecting area." For imaging, the critical characteristic is its resolution. In general, we don't know the distance to the objects we are looking at; we can only measure the angle they subtend at the location of the observer. So we use the term "angular" rather than spatial resolution to characterize the imaging capability of a telescope. In principle, the larger the telescope aperture, the better is its inherent resolution. However, in practice, telescopes operating on the ground, observing through the Earth's turbulent atmosphere, are limited by atmospheric turbulence.